ADVANCED ELECTRONIC MATERIALS Open Access
www.advelectronicmat.de

Automated Scanning Dielectric Microscopy Toolbox for Operando Nanoscale Electrical Characterization of Electrolyte-Gated Organic Transistors

Shubham Tanwar, Ruben Millan-Solsona, Sara Ruiz-Molina, Marta Mas-Torrent, Adrica Kyndiah, and Gabriel Gomila**

Electrolyte-gated organic transistors (EGOTs) leveraging organic semiconductors' electronic and ionic transport characteristics are the key enablers for many biosensing and bioelectronic applications that can selectively sense, record, and monitor different biological and biochemical processes at the nanoscale and translate them into macroscopic electrical signals. Understanding such transduction mechanisms requires multiscale characterization tools to comprehensively probe local electrical properties and link them with device behavior across various bias points. Here, an automated scanning dielectric microscopy toolbox is demonstrated that performs operando in-liquid scanning dielectric microscopy measurements on functional EGOTs and carries out extensive data analysis to unravel the evolution of local electrical properties in minute detail. This paper emphasizes critical experimental considerations permitting standardized, accurate, and reproducible data acquisition. The developed approach is validated with EGOTs based on blends of organic small molecule semiconductor and insulating polymer that work as accumulation-mode field-effect transistors. Furthermore, the degradation of local electrical characteristics at high gate voltages is probed, which is apparently driven by the destruction of local crystalline order due to undesirable electrochemical swelling of the organic semiconducting material near the source electrode edge. The developed approach paves the way for systematic probing of EGOT-based technologies for targeted optimization and fundamental understanding.

1. Introduction

Localized physical and chemical processes occurring at the semiconductor/electrolyte, or the gate/electrolyte interface are at the basis of the signal response of many biosensing[1–4] and bioelectronic[5–11] technologies based on electrolyte-gated organic transistors (EGOTs). EGOTs provide the right physiological environment for such processes and can amplify small electrical variations at their interfaces to measurable source-drain current modulations, making them ideal for detecting weak biological and physiochemical signals. However, the current understanding of the operating and transduction mechanism of EGOTs at the nanoscale is very limited as only a handful of techniques (namely scanning dielectric microscopy,[12] scanning electrochemical microscopy,[13] scanning strain microscopy,[14] and bimodal atomic force microscopy).[15] have been able to probe relevant local physical properties (conductivity,[12]

S. Tanwar, R. Millan-Solsona, G. Gomila
Nanoscale Bioelectrical Characterization Group
Institut de Bioenginyeria de Catalunya (IBEC)
The Barcelona Institute of Science and Technology (BIST)
Carrer Baldiri i Reixac 11-15, Barcelona 08028, Spain
E-mail: stanwar@ibecbarcelona.eu; gabriel.gomila@ub.edu

R. Millan-Solsona, G. Gomila
Department d'Enginyeria Electrònica i Biomèdica
Universitat de Barcelona
Carrer Martí i Franquès, 1, Barcelona 08028, Spain

S. Ruiz-Molina, M. Mas-Torrent
Institut de Ciència de Materials de Barcelona (ICMAB-CSIC)
Campus UAB Cerdanyola del Vallès, Barcelona 08193, Spain

A. Kyndiah
Center for Nano Science and Technology
Istituto Italiano di Tecnologia
Via Rubattino 81, Milano 20134, Italy

The ORCID identification number(s) for the author(s) of this article can be found under https://doi.org/10.1002/aelm.202400222

DOI: 10.1002/aelm.202400222

interfacial capacitance,[12] electrochemical potential,[13] ionic transport,[14] dynamic topographic changes and nanomechanical properties)[15] in an electrolyte environment under biased conditions. Kyndiah et al. implemented in-liquid scanning dielectric microscopy (SDM) to probe the semiconductor/electrolyte interface in operating electrolyte-gated organic field-effect transistors (EGOFET—an EGOT with ion-impermeable semiconductor) and showed that the measured local electrostatic forces are sensitive to the local conductivity and interfacial capacitance of the semiconductor.[12] The technique proved to be extremely sensitive to the presence of ultrathin (≈1 nm thick) skin dielectric layers, which sometimes results from a vertical phase separation phenomenon[16–19] common in blended thin films. The possibility to derive the local electric potential distribution by means of this technique was later demonstrated in ref. [20]. On the other hand, scanning electrochemical microscopy (SECM) showed sensitivity to the local electrochemical potential,[13] electrochemical strain microscopy (ESM) to the local dynamic volumetric swelling due to ion uptake,[14] and bimodal AFM to local nanomechanical properties[15] in organic mixed ionic-electronic conductors, and hence are also promising tools for understanding the underlying fundamental ionic and electronic processes.

We highlight that many of the reported studies[14,15,21,22] have focused on probing the semiconductor that is uniformly coated on an electrode, without any electric current flow along it, which differs greatly from the conditions present in a three terminal EGOT device. In EGOTs, an applied drain voltage results in an electric potential gradient that causes substantial spatial variations in the local physical properties. The global device response then originates from charge carriers traversing this potential landscape through heterogenous macroscale percolative pathways between the source and drain electrodes. Therefore, understanding the charge transport in EGOTs warrants direct probing of the semiconductor/electrolyte interface throughout the device's active area bridging source and drain electrodes under both gate and drain applied biases.

Existing scanning probe microscopy techniques for in-operando studies in EGOFETs still lack wide adoption due to challenges in i) the integration of functional devices, ii) the complexity of the experimental setups, iii) the slow nature of the measurements owing to the manual user operation and iv) the need to explore a wide range of operating points and conditions (ideally hundreds of them) corresponding to the several combinations of source and drain voltages necessary to probe the different operating regimes and their unique distributions of the local properties that distinctly affect the macroscale response.

To address these challenges, here we report the development of an automated scanning dielectric microscopy toolbox and methodology that standardizes the implementation of in-liquid SDM on operating electrolyte-gated transistors for comprehensive functional imaging across different operating regimes. In the developed methodology, we also propose strategies to remove high-frequency artifacts pertaining to in-liquid SDM measurements that could severely impact data reproducibility in automated workflows.[23] We then validated the automated setup by thoroughly mapping the evolution of local electrical properties of two different functional p-type accumulation mode EGOFET based on blends of organic small molecule semiconductor with an insulating polymer, namely (i) a blend of diF-TES-ADT [2,8-difluoro-5,11-bis(triethylsilylethynyl) anthradithiophene] and an insulating polymer polystyrene (PS), and (ii) a blend of TIPS-pentacene [6,13-bis(triisopropylsilylethynyl)pentacene] and polystyrene (PS). Further, we performed the automated nanoscale reliability assessment of one of these EGOFETs (diF-TES-ADT:PS) at high gate voltages, shedding light on its degradation mechanism and indicating a "safe" operating window for such devices. The proposed automated workflow could fast-track the development process of design and operational rules for new materials and devices for a wide range of applications.

2. Results and Discussion

2.1. Automated Scanning Dielectric Microscopy Setup for EGOTs Nanoscale Functional Probing

In scanning dielectric microscopy, an amplitude-modulated AC voltage of frequency, f_{el}, in the 10s of MHz range, and modulation frequency, f_{mod}, in the kHz range is applied to a conductive AFM probe.[24] At such high frequencies (beyond the dielectric relaxation frequency of the electrolyte), the AC electric force acting on the probe is not screened by the ionic space charge layers and is sensitive to the local polarization/conductive properties of the sample surface. In the developed system, the electrolyte-gated transistor (EGOT) is integrated onto the sample stage of the SDM by using retrofitted electrical point probes for applying DC bias voltages, as schematically shown in **Figure 1**A and photographically in S1 (Supporting Information). The point probes provide stable electrical connections for long-term measurements, as well as the flexibility of integrating EGOTs of different designs and geometries. The EGOT is biased at the desired operating point by applying drain (V_{DS}) and gate (V_{GS}) voltages as indicated in Figure 1A (the source is set to ground). The SDM probe coated with platinum (or gold) acts both as the gate electrode and the force sensor, and hence it is connected to a DC gate voltage on top of which the high-frequency amplitude-modulated waveform is applied to enable the detection of local electrostatic forces sensitive to the local conductivity and interfacial capacitance as detailed elsewhere.[12] An additional external gate electrode of a different material can also be introduced if required at which only a DC gate voltage is applied. The rationale behind this double gating approach is to allow the flexibility of using the external gate electrode of any material to gate the transistor and not be limited by the availability of an appropriate AFM cantilever as in the previous implementation.[12] The use of two gate electrodes can shift the threshold voltage, but without affecting the intrinsic performance or stability of the semiconducting material.

The network of instruments and respective connections are highlighted in Figure 1B. It includes a computer running the automation routines (1), the source measuring unit (SMU) (2), the radio frequency (RF) function generator (3), an oscilloscope (4), a lock-in amplifier (5), and the AFM electronics and PC (6). The set-up includes, in addition, an optical microscope (not shown in Figure 1) onto which the scanning probe microscope is mounted (see Figure S1.1, Supporting Information).

The typical experimental workflow is illustrated in Figure 1C and described below in detail:

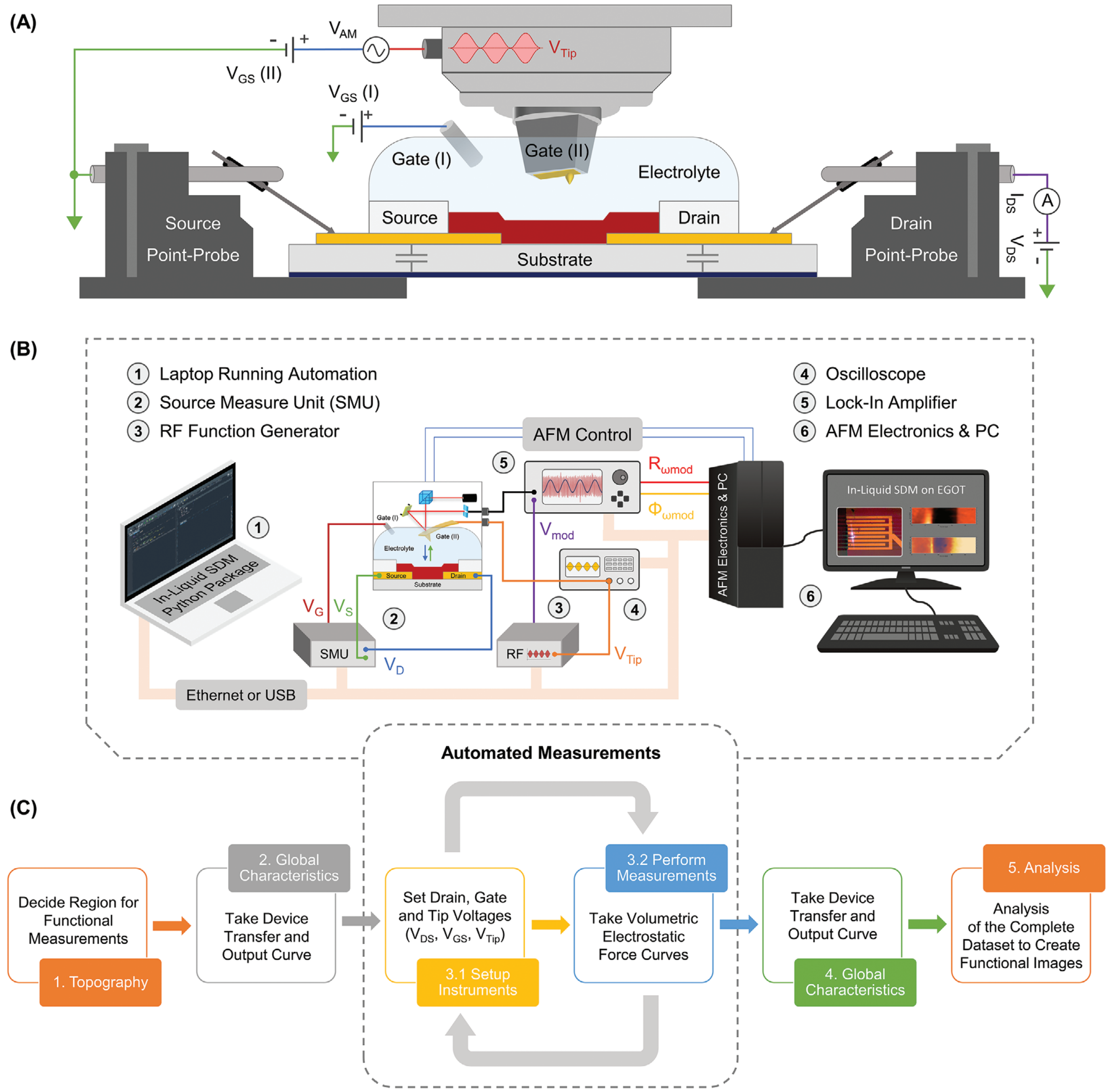

Figure 1. Automated in-liquid SDM setup for operando EGOT nanoscale functional characterization. A) Schematic of the in-liquid SDM implementation on operating electrolyte-gated transistors. B) Network of instruments indicating connections among various instruments, AFM PC and a laptop running *EGOTinLiquidSDM* Python automation scripts. C) A typical measurement protocol with automated data acquisition workflow for successive measurements at different drain and gate voltages.

1) First, a representative region of the device spanning the source-channel-drain area is selected by the user based on an optical and/or AFM topographic image.
2) The standard transfer and output characteristics of the EGOT are measured with the SMU in the configuration shown in Figure 1A. These curves aid in defining the transfer characteristics and charge transport parameters, such as threshold voltage (V_{TH}) at time t_0 before starting the SDM measurements. Moreover, the transfer curve can be compared with the reconstructed characteristics from the in-operando drain current versus time measurements to affirm the stability of the device. These curves are referred to as pre-operando I–V characteristics in our measurements. Sometimes, this step can be skipped depending on the goal of the experiments. For example, if the main goal is to study the hydration phenomena of the semiconductor during operation, as in most cases in organic electrochemical transistors (OECT), then the transfer curve at time t_0 is not acquired.

3) Automated in-liquid SDM nanoscale measurements are then performed at different drain and gate voltages on the selected region. The sub-sequence of automated operations involved are:
   i) Apply DC bias voltages (gate and drain voltage) to the EGOT and the amplitude-modulated waveform with the DC offset (gate voltage) to the SDM probe. The drain and gate currents are continuously recorded. The applied voltages to the tip can be checked with the oscilloscope, whose peak-to-peak amplitude is also recorded. After applying voltages, one waits a set time (10-30 s) for the EGOT to reach a steady state. This specific wait time is determined from the drain current versus time recording at fixed applied biases and depends on the time response of the device, which could vary and requires user adjustments for EGOTs based on different active materials and electrolyte concentrations.
   ii) Approach the SDM probe on the surface of the EGOT and wait a set time (instrument-specific) for the approach to finish after giving the command (≈5 s).
   iii) Start scanning the selected region of the transistor by recording approach curves of the deflection and oscillation amplitude at the modulation frequency at each pixel in the imaged area using the so-called Quantitative Imaging mode of the JPK BioAFM adapted to SDM.[25] Similar modes can be implemented in other AFMs from different manufacturers.
   iv) Once the scan is finished, retract the tip and wait a set time (instrument-specific) for the retract to finish (≈5 s). Also, sometimes, an additional wait time (≈5 s) is used as a buffer in case the previous operations take longer than expected.
   v) Turn off all the applied voltages and save the drain and gate current recordings versus time and the in-liquid SDM approach curves dataset with the appropriate labels.
   vi) Plot and perform preliminary data analysis.
   vii) Repeat (i) to (vi) for different DC bias voltages.
4) Measure transfer and output characteristics of the device as taken in step 2. These measurements are referred to as post-operando I–V characteristics.
5) Perform comprehensive data analysis of the whole dataset with custom-developed Python scripts to produce topographic and electric force images in different modes (lift-mode or constant height mode),[25] as well as functional images of the electric potential[20] and of the conductivity and interfacial capacitance[12] upon proper quantitative analysis for the latter.

The automated process in step 3 (see implementation details in the Experimental Section) aids in a comprehensive probing of EGOTs in a wide range of biasing conditions and establishes in-liquid SDM as a preferred tool for multiscale measurements while inflicting standardized, reliable, and reproducible data acquisition strategies. The data throughput is substantially increased with the automated workflow. Initially, with manual user operations, only a few 10s of operando in-liquid SDM images could be taken in a workday due to labor-intensive user operations required as described above to get a data set for one voltage bias, which increases in multiples as the number of operating points to explore increases. The automated routines implemented in Python take care of all the user operations defined in step 3 except for occasional instances to adjust the scan region in case of drifts in the system. Some steps can be taken to minimize drifts in long experiments, such as keeping the piezo offset close to zero by carefully centering the device at the center of the instrument imaging range, adjusting the tilt of the AFM scanner to be parallel to the sample surface, and releasing the tension in the point probe touching the device by tapping on it before the start of the first measurement. With such considerations and automation, hundreds of bias points and force curves data sets and images can be consistently taken in a workday (8–10 h), giving approximately a 10-fold increase in data and productivity. This allows us to routinely probe the transistor over a wide range of V_{GS} and V_{DS} values. The Python routines are bundled in a custom package named "EGOTinLiquidSDM" (see code availability section), which handles communication between different instruments (JPK BioAFM, source measuring unit, RF generator, lock-in amplifier, and oscilloscope). The developed Python package has different modules for different operations and can be executed in any feasible order according to the experiment's requirements, providing flexibility and reusability of codes. A set of dedicated data analysis scripts has also been developed, which perform extended data analysis to extract images of the sample topography and electric force, as well as potential maps following the methods developed in ref. [20]. Additionally, a MATLAB code is used for the quantitative analysis of the conductivity and interfacial capacitance, following the methods presented earlier,[12] but adapted to work with relative electrostatic force variation curves (see below).

2.2. Correction of High-Frequency Artifacts

The semiconductor evolves from practically insulating (off-state) to highly conductive (on-state) regions as the in-liquid SDM measurements span various operating regimes. As a result, the probe sample impedance experiences a large variation in its value, which can introduce artifacts associated with the high frequencies (10s of MHz) used in the in-liquid SDM measurements. For this reason, corrections of high-frequency artifacts are mandatory for reliable, reproducible, and accurate probing of EGOTs by in-liquid SDM.

The measured electrostatic force in in-liquid SDM originates from the applied high-frequency voltage that drops within the electrolyte solution gap between the tip and the sample. The portion of the potential dropped in this gap with respect to the total tip-sample applied voltage depends on the conductivity and thickness of the semiconductor, the interfacial Stern capacitance of the tip and semiconductor, the conductivity of the electrolyte solution and the substrate underneath the semiconductor. But in implementations of in-liquid SDM, the actual potential drop is also affected by other factors, which may induce some artifacts in the measurements. For instance, the source and drain external circuits are not equivalent at high frequencies due to asymmetric electrical connections that lead to spatial variation in the potential drop within the solution gap, which may appear as a significant slope in the acquired electrostatic force image or highly asymmetric force on the source and drain even for zero applied source-drain voltage. Moreover, the EGOT exhibits dynamic electrical behavior as a function of applied drain and gate voltages due to changes in conductivity distribution and thus represents a dynamic impedance between the SDM probe and the whole transistor. This dynamic impedance can lead to variations in the total AC tip-sample high frequency voltage, which is generally assumed constant. The AC tip-sample voltage can also have spatial variability as the probe traverses the source-channel-drain region depending on the measurement frequency, device footprint, substrate type, and external electrical connections. Therefore, these two artifacts must be corrected separately to obtain reliable measurements with in-liquid SDM.

Figure 2 illustrates the convolution of these two measurement artifacts along with their corresponding remedies. As a testbed, we used p-type accumulation mode EGOFET based on a blend (diF-TES-ADT:PS) of the organic small molecule semiconductors diF-TES-ADT [2,8-difluoro-5,11-bis(triethylsilylethynyl) anthradithiophene] with an insulating polymer polystyrene (PS). We examined different configurations of the external electrical connections where the difference is in terms of the ground reference for the high-frequency tip voltage. Figure 2A shows a schematic of the measurement configuration when the high-frequency tip voltage is applied with reference to the E1 electrode with a DC offset (V_{GS}), i.e., in this case, the E1 electrode is the “source” terminal. A drain voltage (V_{DS}) can be applied by the SMU between the E1 and E2 electrode if desired. The stray capacitances due to the underlying substrate ($\mathrm{SiO_2}$/Si++) are also highlighted with the equivalent coupling capacitance of $C_{\mathrm{sub,eq}}$ between the source and the drain electrodes. In this configuration with $V_{GS} = 0$ V and $V_{DS} = 0$ V, i.e., OFF-state, the absolute electrostatic force image (Figure 2B) is recorded spanning source-channel-drain region at 7 MHz frequency and represented in terms of the absolute tip-sample capacitance gradient. The resulting image is highly asymmetric, with the source showing significantly higher values than the drain (see image profile in Figure 2C), which is not expected if the electrostatic force is intended to mirror the local conductivity as both the source and drain are at the same voltage. Instead, the asymmetry here arises from the asymmetric source and drain external circuit connections and insufficient capacitive coupling between them at the measurement frequency. The capacitive coupling between source and drain electrodes, mediated by $C_{\mathrm{sub,eq}}$, depends heavily on the nature of the substrate. The stray coupling capacitance ($C_{\mathrm{sub,eq}}$) present determines the frequency up to which the external circuit asymmetry dominates, above which another artifact plays a dominant role, which is discussed below. The choice of frequency (7 MHz) for the measurements above is to highlight one artifact at a time. To note, the difference observed in the electrostatic force on the electrodes and on the channel area is expected due to the difference in the underlying substrate;[12] however, a slope in the channel area for $V_{\mathrm{DS}} = 0$ V in this configuration is an artifact, as mentioned earlier. We examined another measurement configuration in Figure 2D where the tip voltage is referenced with respect to the E2 electrode instead of E1 as in the previous configuration, i.e., the connections are flipped. The corresponding absolute electrostatic force image (Figure 2E) and profile (Figure 2F) show that the asymmetry is flipped as well, which represents that the recorded absolute electrostatic forces are affected by the external electrical connections. The reason for the observed behavior in the configuration of Figure 2A is that when the SDM probe is over the E2 electrode, the segment from the E2 terminal to the high-frequency ground (E1 terminal) takes up a big portion of the applied AC potential for that measurement frequency, leaving a very low AC potential drop within the solution gap and thus resulting in a low electrostatic force. Concurrently, a change in the tip-sample impedance as the tip traverses the source-channel-drain region causes an AC tip-voltage change (discussed below), thereby further exaggerating the asymmetry in the measured electrostatic force. A similar explanation holds for the configuration in Figure 2D. This artifact can be removed by simply putting an external capacitor between the source and drain electrodes that capacitively couples them only at the MHz frequencies of in-liquid SDM measurements without affecting the DC operation of the EGOT. The value (100 nF) of the external capacitor is chosen in order to provide an electrical short (<1 Ω) between source and drain electrode at the measurement frequency, and it is also readily available in the labs. Figure 2G shows this configuration and the corresponding absolute electrostatic force image (Figure 2H) and profile (Figure 2I), which are symmetric as intended. However, one more artifact remains in these measurements, which needs to be corrected to finally achieve artifact free representation of the measured electrostatic force data, as discussed below.

The second artifact of tip-voltage change, i.e., due to changes in the tip-sample impedance, can be illustrated with measurements done at different frequencies for the three configurations (Figure 2J–L). Each line in the images is scanned at a different high-frequency voltage ranging from 1 MHz (bottom) to 119 MHz (top). The change in frequency causes a change in tip-sample impedance and hence tip-sample voltage owing to standing wave formation due to high-frequency reflections at the tip-sample junction. At certain frequencies, due to coaxial resonance, the AC voltage arriving at the tip maximizes, which leads to an increase in the measured electrostatic force. In the studied EGOFET structure, at sufficiently high frequencies, the absolute value of the force decreases substantially (see the dark blue region in Figure 2J–L), which probably indicates a reduced transfer of power from the RF source to the tip. The absolute force frequency spectrum depends on numerous geometrical and physical parameters of the system and does not reflect any true electrical property of the semiconductor, as one would intend. For example, S2 (Supporting Information) shows similar measurements as of Figure 2 on the same transistor but on a glass substrate instead of a $\mathrm{SiO_2}$/Si++ substrate. The measured absolute force frequency spectrum is systematically different, due to differences in the stray coupling capacitance ($C_{\mathrm{sub,eq}}$) mediated by the substrate. Nonetheless, these frequency measurements emulate the impact of changing tip voltage on the measured absolute force. In practice, we generally do measurements at one frequency and this kind of tip-voltage change artifact will come into play when different drain and gate voltages are applied, which changes the conductivity distribution of the semiconductor and, consequently, the tip-sample impedance and, thus the AC potential arriving at the tip, thereby severely masking the actual trends. To tackle this artifact, a renormalization factor was introduced in earlier approaches.[12,26] However, applying the same renormalization procedure to a dynamic system like an EGOT is impractical, primarily due to spatial variability

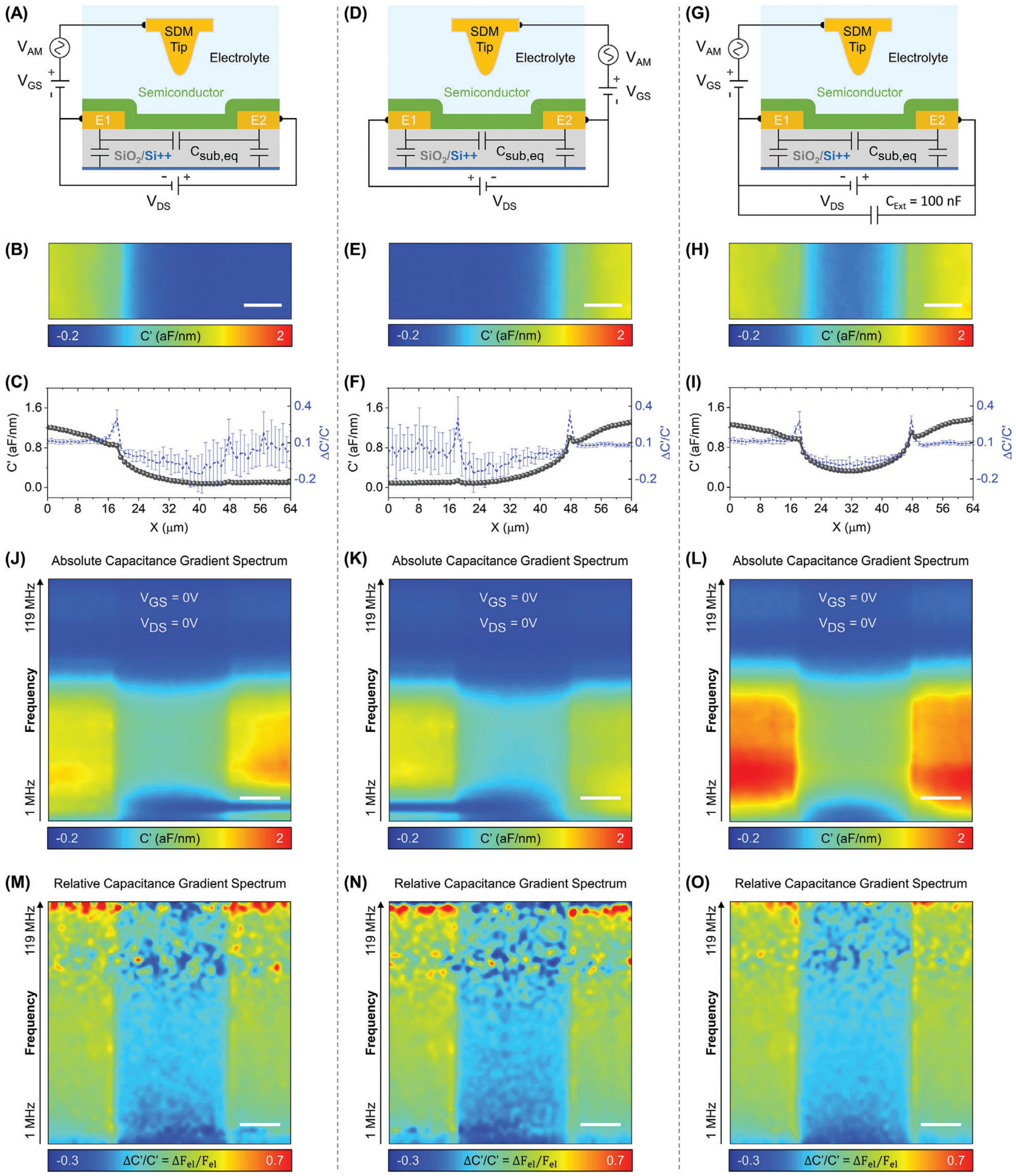

Figure 2. Correction of high-frequency artifacts. A) Schematic of an in-liquid SDM configuration with the tip biased with respect to electrode E1 and drain voltage applied between electrode E1 and E2. B) Absolute electrostatic force lift-mode (Z_{lift} = 100 nm) image of an area spanning source(E1)-channel–drain(E2) region for $V_{GS} = 0$ V and $V_{DS} = 0$ V. C) (symbols and continuous black line) Absolute and (dashed blue line) corresponding relative electrostatic force lift-mode profile averaged in the vertical direction of the image in (B). D–F) Idem to A–C) but with the tip referenced to the electrode E2. G–I) Idem to A–C) but with an additional external coupling capacitor (100 nF) between the electrodes E1 and E2. J) Absolute electrostatic force lift-mode image spectrum where at each scan line the frequency of the high-frequency signal is changed starting from 1 MHz and ending at 119 MHz, measured in the configuration shown in (A). K) Idem to J) but measured in the configuration shown in (B). L) Idem to J) but measured in the configuration shown in (C). M) Relative electrostatic force image spectrum (Z_{lift} = 100 nm and Z_{ref} = 1600 nm) corresponding to J), N) corresponding to K), and O) corresponding to L). The scale bar is 10 μm. Experimental parameters: Electrolyte = 1×10^{-3} M NaCl, SDM Probe = HQ:NSC19/Cr-Au, f_{el} = 7 MHz for B,E,H), f_{mod} = 10 kHz, V_{ac} = 4 VPP, pixels 64 × 20 (64 × 20 μm^2) for B,E,H) and pixel 60 × 60 (60 × 60 μm^2) for J)-O), k = 1.16 N m^{-1}, f_{res} = 35.60 kHz (cantilever).

mandating deriving different factors for each electric force approach curve at each pixel and for each operating point. Furthermore, the automation developed here generating hundreds of electrical images makes the renormalization approach completely unfeasible. Surprisingly, we found a robust and straightforward method to remove this tip-voltage change artifact entirely during data processing directly on raw data, which involves simply taking the relative electrostatic force variation with respect to far-away reference tip-sample distance in an electric force approach curve, i.e., $(F_{\mathrm{el},Z_{\mathrm{lift}}} - F_{\mathrm{el},Z_{\mathrm{ref}}})/F_{\mathrm{el},Z_{\mathrm{ref}}}$, allowing fast accurate qualitative and quantitative analysis. Figure 2M–O shows the relative electrostatic force images corresponding to the absolute electrostatic force images shown in Figure 2J–L respectively. We have also overlayed relative electrostatic force profiles corresponding to Figure 2B,E,H in Figure 2C,F,I, respectively. The tip-voltage change artifact is completely removed. It is important to note that complete artifact-free representation of the measured electrostatic force data with high signal-to-noise ratio emerges only for the case when there is a significant coupling between source and drain electrodes at the measurement frequency (see, for example, Figure 2I in comparison to Figure 2C,F). After considering relative variation, the electrostatic force is independent of frequency as expected (as long as it is above the dielectric relaxation frequency of the electrolyte and below the dielectric relaxation of the semiconductor material). The noisy structure in the frequency spectrum of relative electrostatic force images at higher frequencies is due to the low signal-to-noise ratio as the amplitude of absolute electrostatic force is small (see dark blue region in Figure 2J–L). The underlying rationale behind this relative approach is that the relative portion of applied potential drop within the solution remains the same even if the total AC tip-sample voltage is changed as long as no other electrically relevant parameter of the system is changing. Any local change in the relative electrostatic force with changing DC bias voltages will thus reflect the change in semiconductor conductivity as one eventually intended. Therefore, throughout the paper, measurements are done in the configuration shown in Figure 2G and relative electrostatic force images are plotted and referred to as just electrostatic force images otherwise noted.

The easy and straightforward approach presented here for correcting these high-frequency artifacts will be instrumental for reproducible and reliable measurements with automated systems where hundreds of images are generated, and especially in future for building completely autonomous characterization and discovery platforms.[23]

2.3. Validating Automated Workflow for Operando Characterization of Functional EGOFETs

We validated the developed operando in-liquid SDM set-up and automated workflow by comprehensively probing the nanoscale electrical characteristics of the EGOFET devices described in the previous section. In a previous work, diF-TES-ADT:PS blend has been used to produce EGOFETs to develop a stable bioelectronic recording platform for excitable cells[8] and as test platform to demonstrate the capabilities of operando in-liquid SDM.[12,20]

Figure 3A shows the topography and profile of a 60 × 10 μm^2 area spanning source-channel-drain region before the application of any bias voltage, where we later performed the automated local electrical measurements at different drain and gate voltages. The EGOFET consists of interdigitated source–drain electrodes with a nominal channel length L = 30 μm, an effective channel width W = 19680 μm ($W/L = 656$), and a nominal semiconductor thickness h_{sem} = 30 nm (which can be verified from a topographic hole near the source edge). Figure 3B shows the reconstructed transfer curve obtained from the operando drain currents recorded during in-liquid SDM measurements (see S3, Supporting Information and Figure S3.1, Supporting Information), representing the expected accumulation mode of operation. These reconstructed transfer curves are consistent with the pre-operando curves recorded before starting the nanoscale measurements (see Figure 3B).

Figure 3C shows the (relative variation) electrostatic force images obtained at different drain voltages V_{DS} = 0, −0.1, −0.2, −0.3 V, and gate voltages (V_{GS}) changing from 0.2 to −0.8 V in steps of −0.02 V, giving rise to a total of 51 images per drain voltage and an overall number of 204 images. At each operating point, according to the sequence of operations defined in step 3 in the previous section, the wait time for step 3(i) is set at 10 s and for step 3(ii) is set at 5 s, to allow the transistor to reach a steady state before starting the functional imaging (see Figure S3.1, Supporting Information). An approach curve dataset for a single voltage takes ≈51 s for a 60 × 10 pixel image, which results in 84 ms for a single-pixel approach curve. After an image is taken, the tip is retracted, and voltages are turned off after a wait of 5 s (step 3-iv). Overall, a single measurement is completed in 1 min 16 s including wait and buffer (additional 5 s) time periods, and all measurements for one drain voltage dataset (N = 51) are completed in approximately 1 h 5 min, and the full sets of data are acquired in 4 h 20 min. It is important to note that an equivalent sets of data would take few workdays if done manually due to the time spent separately controlling each instrument along with manually saving data with appropriate labels. The most cumbersome task to do manually is synchronizing and tracking the exact wait time between operations, which in practice needs to be adjusted to a longer duration to be feasible. With automation, all these practical challenges are completely removed, while increasing the data throughput substantially. Topographic images are also obtained for each pair of voltages probed (see Figure S3.2, Supporting Information). In the present case, no variation is observed in the topography with applied voltages.

Figure 3D–F shows the averaged evolution of local electrostatic force over the source, channel, and drain regions respectively as a function of gate voltage and for the different drain voltages, built from images in Figure 3C. The electrostatic force starts increasing in the channel at V_{GS} roughly equal to the device's threshold voltage (see Figure 3B for transfer curves). Over the drain electrode, the curves start shifting by an amount roughly equal to the applied drain voltage as described earlier.[20] To extract quantitative local functional properties of the device from the measured electric force data, one can use the procedure detailed in ref. [12] to obtain the local conductivity/interfacial capacitance distributions or that detailed in ref. [20] to obtain the local potential distribution. In S4 (Supporting Information), we present the quantitative conductivity analysis corresponding to the data of Figure 3, together with the details for its implementation to the case of relative electrostatic force variation data, not provided earlier.

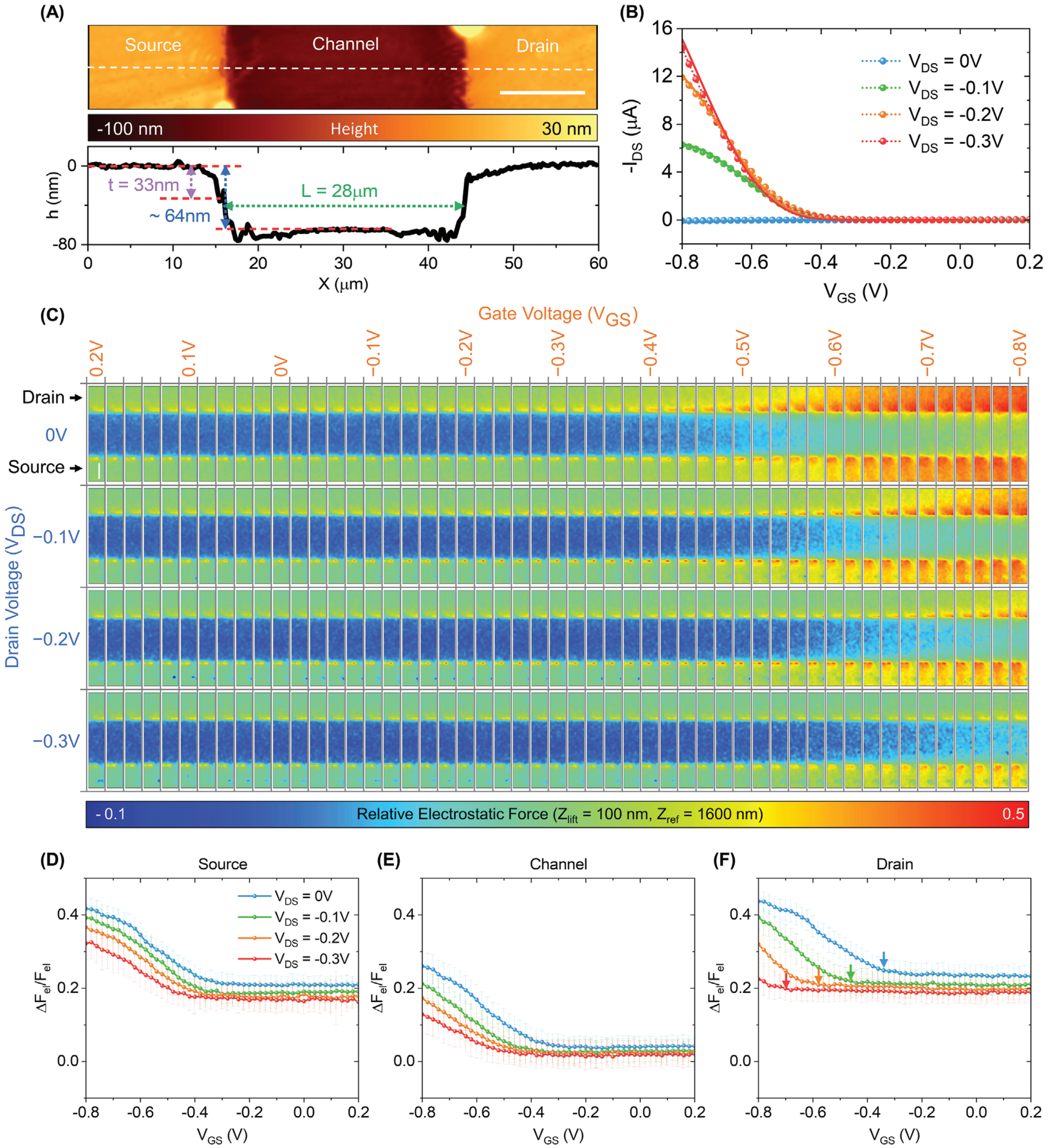

Figure 3. Validation of the automated in-liquid SDM workflow for operando characterization of a functional EGOFET. A) AFM topography of a 60 × 10 μm^2 area of the EGOFET transistor based on diF-TES-ADT:PS blend, showing source, channel, and drain regions along with the topographic profile. B) (continuous lines) pre-operando transfer curve, (symbols and dotted lines) drain current versus gate voltage transfer curves reconstructed from the drain current recording during operando measurements (see Figure S3.1, Supporting Information). C) Relative electrostatic force lift-mode images (Z_{lift} = 100 nm and Z_{ref} = 1600 nm) for V_{DS} = 0, −0.1, −0.2, and −0.3 V and V_{GS} from 0.2 to −0.8 V in steps of −0.02 V. D–F) Averaged local electrostatic force versus gate voltage curves for the source, channel and drain region respectively, built from the dataset in (C). The scale bar is 10 μm. Experimental parameters for in-liquid SDM measurements: Electrolyte = 1 × 10^{-3} M NaCl, Gate = Au SDM Probe (HQ:NSC19/Cr-Au) + Pt external electrode, f_{el} = 25 MHz, f_{mod} = 10 kHz, V_{ac} = 3 VPP, pixels 60 × 10, k = 0.57 N m^{-1}, f_{res} = 26.44 kHz (cantilever).

Similarly, we have further validated the developed approach on an EGOFET of same architecture but based on a different blend (TIPS-pentacene:PS) and performed quantitative analysis by deriving local electric potential maps following the procedure detailed elsewhere[20] (see S5, Supporting Information for operando measurements and its analysis). These measurements and quantitative analysis validate the automated workflow for the operando characterization of functional EGOT devices and reliably capture the evolution of local electrical properties.

2.4. Automated Nanoscale Reliability Assessment of Functional EGOFETs

After validating the automated in-liquid SDM workflow for in-operando nanoscale electrical characterization of EGOFETs, we further use it to perform their reliability assessment under operational conditions. We used EGOFETs based on the diF-TES-ADT:PS blend as in the previous section but with shorter channel length (L = 10 µm) and explored their reliability across extended gate voltage range (V_{GS} from 0.2 to −1.0 V) in different sweep cycles, namely, Cycle 1—Forward (**Figure 4** and supporting information S6), Cycle 2—Backward (supporting information S7), and Cycle 3—Forward again (supporting information S8). Figure 4A shows the initial topography before applying any bias voltage to the device of a region of an EGOFET device spanning the source-channel-drain region (24 × 6 µm^2) where automated in-liquid SDM measurements are to be performed (see Figure 4B for the corresponding topographic profile). The EGOFET consists of interdigitated source–drain electrodes with a nominal channel length L = 10 µm, an effective channel width W = 6560 µm (W/L = 656), and a nominal semiconductor thickness h_{sem} = 30 nm. Figure 4C shows the relative electrostatic force images obtained from the electrostatic force approach curve data sets for a lift distance Z_{lift} = 100 nm and Z_{ref} = 2000 nm, at a drain voltage V_{DS} = −0.1 V and gate voltages (V_{GS}) changing from 0.2 to −1.0 V in steps of −0.02 V, giving rise to a total of 61 images. At each operating point, according to the sequence of operations defined in step 3 in the previous section, the wait time for step 3(i) is set at 10 s, and for step 3(ii) is set at 5 s to allow the transistor to reach a steady state before starting the functional imaging. A single image takes 86 s for a 64 × 16 pixel image, which results in 84 ms for a single-pixel approach curve. After an image is taken, the tip is retracted, and voltages are turned off after a wait of 5 s (step 3-iv). Overall, a single measurement is completed in 1 min 46 s, including wait time periods, and all measurements (N = 61) are completed in approximately 2 h considering some buffer time.

The (relative) electrostatic force on the source in the images in Figure 4C at first stays low in the sub-threshold regime and then starts increasing at around −0.04 V (see Figure S6.1, Supporting Information, for relative electrostatic force versus gate voltage local transfer curve for clarity) which is the local threshold voltage, while on the drain electrode, the electrostatic force starts increasing only from −0.14 V onwards due to the applied drain voltage (V_{DS} = −0.1 V) increasing the local threshold voltage at the drain. The channel also shows an increase in electrostatic force with increasing gate voltage, while showing initially some slope in the channel region due to the spatial variation in the local conductivity owing to the applied drain voltage. As the gate voltage continues to increase, we notice that the electrostatic force becomes uniform across the device due to the sensitivity limit of the in-liquid SDM, i.e., the conductivity has increased to a level that for the SDM probe everything is like a metal, whether it is over the channel or electrode. Interestingly, this condition of uniform force across the device due to high conductivity of the semiconducting material is not reached in long-channel devices (L = 30 µm) as shown earlier and in previous reports,[12,20] which points towards comparatively better performance of these short-channel (L = 10 µm) devices. The thin film of this blend (diF-TES-ADT:PS) in similar devices is known to exhibit heterogeneously oriented crystalline domains of sizes as high as 30 × 30 µm^2 area,[27] which in long channel devices could have significant grain boundaries within the active channel area, thereby potentially acting as a charge transport bottleneck, and consequently decreasing the conductivity values reachable within the operating gate voltage window.[20]

Further, it was observed that upon increasing the gate voltage beyond a certain threshold (< −0.8 V), the local electrostatic force starts decreasing (images within the gray dashed rectangle in Figure 4C). The channel area near the source electrode edge decreases first, followed by the region over the source electrode itself and then ultimately at the drain. The in-operando drain current recording also shows a decrease (see Figure S6.2, Supporting Information, green curve). In addition, the simultaneously acquired topography images (Figure 4D), built from acquired deflection approach curves, show topographic swelling near the source edge. Extended local morphological analysis of these topographic images (see S9, Supporting Information and Figure S9.1, Supporting Information) indicates swelling up to 40 nm near the source edge relative to point on source where there is not much apparent swelling. This corresponds to more than 130% increase than the nominal thickness of the semiconductor (30 nm), which indicates significant non-uniform disruption in the crystalline order of the diF-TES-ADT molecules over the source electrode. In contrast, over the drain and in channel, no such significant changes are observed (Figure S9.1, Supporting Information, Cycle 1—Forward).

We have also analyzed the reversibility of the observed changes. To this end, the same measurements were performed with decreasing gate voltages in the same device from V_{GS} = −1.0 V to V_{GS} = 0.2 V (see S7, Supporting Information and Figure S7.1, Supporting Information, this dataset is collectively referred as Cycle 2—Backward Sweep). We observed that the electrostatic force modulation with gate voltage in this backward cycle is substantially reduced in the channel area in comparison to the initial forward sweep, which is in concurrent agreement with the substantial drop in the measured drain current. The region over the source shows a reduction in electrostatic force, whereas for the drain an increase is observed. At the same time, the corresponding topography images (Figure S7.2, Supporting Information) show that a double-edge feature is seen at the source edge while in the channel some topographic swelling is observed, whereas over the drain, location dependent increase-decrease is observed; refer to Figure S9.1 (Supporting Information) for the extended local morphological analysis. We took high-resolution images on a similar device before and after taking several forward-backward transfer sweeps from V_{GS} = 0.2 V to V_{GS} = −1.0 V, and we

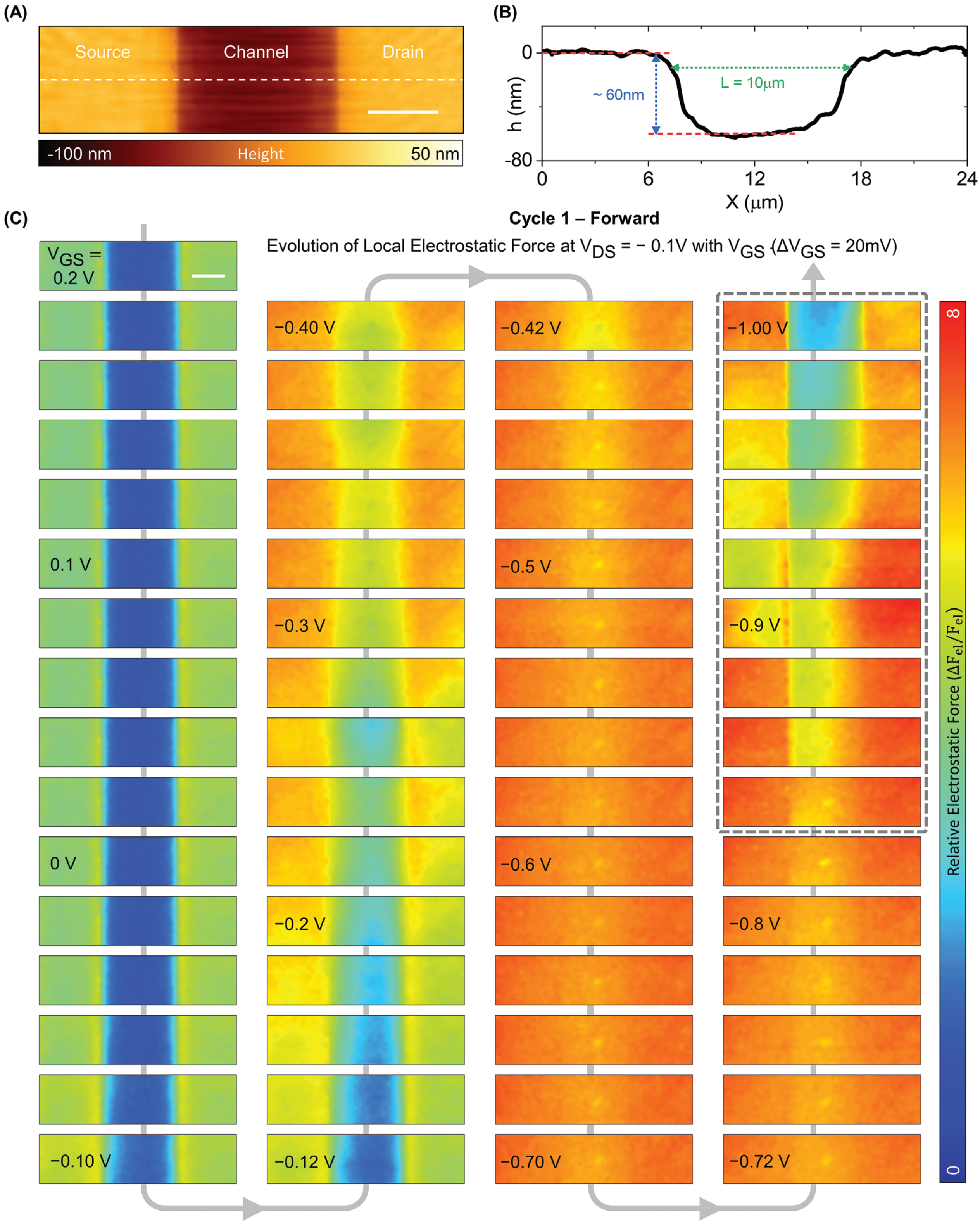

Figure 4. Automated nanoscale reliability operando characterization of functional EGOFET. A) AFM topography of a 24 × 6 μm^2 area of the EGOFET transistor, including source, channel, and drain regions with B) the topographic profile. C) Relative electrostatic force lift-mode images (Z_{lift} = 100 nm and Z_{ref} = 2000 nm) for $V_{\mathrm{DS}} = -0.1$ V and V_{GS} from 0.2 to −1.0 V in steps of −0.02 V. D) Topographic images acquired simultaneously to the electric force images shown in (C). The scale bar is 4 μm. Experimental parameters for in-liquid SDM measurements: Electrolyte = 1 × 10^{-3} M NaCl, Gate = Au SDM probe (HQ:NSC19/Cr-Au) + Pt external electrode, f_{el} = 25 MHz, f_{mod} = 10 kHz, V_{ac} = 2 VPP, pixels 64 × 16, k = 1.162 N m^{-1}, f_{res} = 35.68 kHz (cantilever).

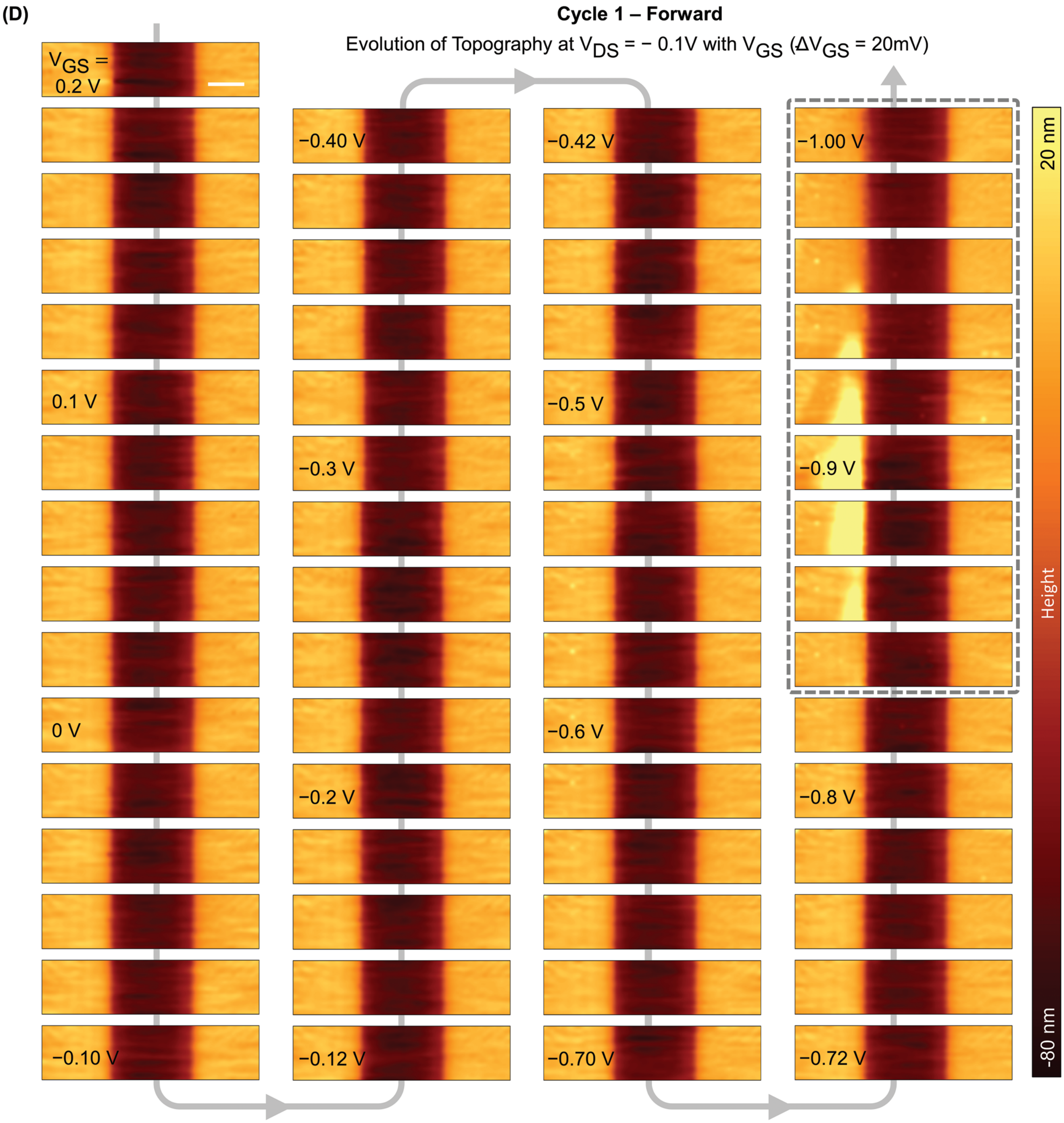

Figure 4. *Continued*

observed that the double-edge feature near the source electrode edge corresponds to stripping of the active semiconducting material (see Figure S9.2), which could result in significant impediment in the flow of drain current and thereby failure of the device.

Another set of measurements in the forward sweep (see S8, Supporting Information and Figures S8.1 and S8.2, Supporting Information, this dataset is collectively referred as Cycle 3—Forward Sweep) reveals the same picture for electrostatic force and no recovery of drain current. Topographically, a swelling is again observed at the source with increasing gate voltage above V_{GS} = −0.8 V (although absent in the backward sweep, cycle 2), which ended ultimately with catastrophic complete delamination of the source electrode from the substrate; see S10, Supporting Information for the optical microscopy images.

The degradation mechanism observed at high gate voltages points towards an electrochemical redox reaction starting at the source electrode that degrades the crystalline order of the semiconducting thin film (vis-à-vis topographic swelling) and leads to stripping of the active semiconducting material at the source electrode edge, which probably leads to the formation of trapping sites for the injected charge carriers, and thereby irreversibly impacts the gate modulation of the conductivity and the integrity of the source electrode. It is important to note that this degradation can be avoided by limiting the gate voltages to −0.8 V maximum, which leads to stable and reversible transistor operation over many hours,[20] as also evident from its use as a stable bioelectronic recording platform for excitable cells.[8] Nonetheless, the automated experimental setup probing the operating device at small bias voltage steps over multiple cycles reveals the evolution of local electrical properties and the spatial onset of the degradation process in minute detail.

3. Discussion on Other Potential Applications

The developed automated nanoscale operando characterization setup capable of investigating electrolyte-gated transistors in operating conditions is indispensable for advancing the field of bioelectronics as it enables systematic studies of relevant nanoscale electrical properties. In general, the developed toolbox is applicable in different aqueous electrolyte solutions, provided high enough frequencies can be transmitted through the system (for typical ionic concentrations $<100 \times 10^{-3}$ м, frequencies in the 100 MHz range are necessary). The automated approaches are particularly helpful where repeated measurements are required as a function of experimental variables, which could be bias voltages as shown here or even time. For example, many biosensing proof-of-concept devices utilize electrolyte-gated transistors for enhanced sensitivity. However, how the nanoscale binding events translate to the amplified electrical device-level signals is often not straightforward to decipher, as many parameters play an important role. An automated characterization setup effectively capable of exploring vast parametric space would be of significant advantage.

In cases where the semiconducting surface is functionalized, the approach presented earlier would directly be able to probe the interface where binding events are happening. However, in most cases, the gate electrode is generally functionalized with a biorecognition layer that detects a specific target analyte. It then becomes essential to envision integration strategies for such applications where the interaction occurs at the gate/electrolyte interface. For example, a potential implementation of automated in-liquid SDM on an EGOT biosensor could involve an extended floating gate architecture where the SDM tip probes the dynamic local electrical characteristics of a functionalized floating gate where biorecognition events occur. In situ and real-time biorecognition events can be simultaneously monitored macroscopically through drain current monitoring in the coupled EGOT. Such potential implementation would allow correlating the local bio-recognition events captured in measured electrostatic force images with EGOT electrical response, thereby providing insights into the transduction mechanism. Since the binding process progresses over time, the automated approach would be instrumental in capturing a time-lapse of the process over various operating points of the device. However, the fabrication and optimization of such architectures is challenging as it requires specific sample holders integrated into the AFM setup, whose discussion is beyond the scope of this paper.

4. Conclusions

In summary, we have presented an automated in-liquid scanning dielectric microscopy (SDM) toolbox for the operando characterization of EGOTs. By implementing this toolbox, we were able to reveal the evolution of their local electrical and morphological properties in minute detail. The automated approach has led to a 10-fold increase in data throughput in comparison to manual user operation, consequently, allowing possibilities for exploring a wider parametric space. For reproducible and accurate measurements, we have addressed and removed the high-frequency artifacts commonly plaguing the dataset and proposed easy and straightforward corrections by simply introducing an external coupling capacitor between source and drain electrodes, and by considering the relative variations in the measured electrostatic force data instead of absolute values. The simplicity of these approaches is particularly advantageous for an automated setup where hundreds of images are need to be analyzed.

We then made use of these developments to comprehensively probe the EGOFETs based on two different blends (diF-TES-ADT:PS and TIPS-pentacene:PS), where we highlighted the subtle changes in local electrical properties and quantified them. Further, we discussed the degradation mechanism observed at high gate voltages for one of these blends (diF-TES-ADT:PS), where probable electrochemical redox reactions originating at the source electrode are degrading the crystalline order of the semiconducting thin film due to undesirable electrochemical swelling, leading to the formation of trapping sites for the injected charge carriers and thereby irreversibly impacting gate modulation of the local conductivity and hampering the integrity of the source electrode.

The present work provides crucial tools and methods for the multiscale comprehensive characterization of operating EGOTs. It is a key step towards establishing structure-property-function relationships, and for formulating design and operational rules for stable and efficient devices for numerous applications in the field of biosensing and bioelectronics.

5. Experimental Section

Electrolyte-Gated Transistor Fabrication: EGOFET devices used for the measurements were fabricated as described elsewhere.[27] Briefly, the device substrate consists of a heavily doped n-type silicon wafer featuring thermal SiO_x (200 nm) on which source and drain electrodes were fabricated by photolithography and thermal evaporation of 5 nm of Cr and 40 nm of Au. The electrodes were functionalized with a self-assembled monolayer of pentafluorothiophenol and thereafter a chlorobenzene solution 2 wt% of diF-TES-ADT, or TIPS-pentacene, and polystyrene (PS) in 4:1 ratio was deposited using the bar-assisted meniscus shearing technique at 10 mm s^{-1} and 105 °C. The EGOFETs on the glass substrate were fabricated following the same procedure.

Automated In-Liquid SDM Setup and Measurements: The present work automates and improves upon an earlier manual implementation of in-liquid SDM on EGOFETs.[12] The automated control and data acquisition and analysis routines are custom developed and implemented in Python (see code availability section). The developed Python package running on a laptop handles the communication between different instruments namely an AFM PC (JPK Nanowizard 4 BioAFM), source-measure unit (Keysight B2912A), RF waveform generator (Keysight 33622A), oscilloscope (Keysight DSOX3024T) and lock-in amplifier (Anfatex eLockIn 204). The instrument connection and measurement protocol are defined in the paper (Figure 1). In a nutshell, it consists of a JPK Nanowizard 4 BioAFM system mounted on a Nikon Eclipse optical microscope and integrating a point probe station (EverBeing EB-700) connected to a Keysight B2912A source measuring unit. The amplitude-modulated AC voltage of amplitude V_{ac}, electrical frequency in the range 1–119 MHz and modulating frequency of 2–10 kHz has been applied by means of the Keysight 33622A RF waveform generator, while the photodiode oscillation signal has been recorded with an external lock-in amplifier (eLockin 204/2, Anfatec). The AFM data acquisition is done in advanced quantitative imaging (JPK) mode. HQ:NSC19/Cr-Au ($k \approx 1$ N m^{-1}, $f_{ref} \approx 35$ kHz in liquid) AFM tips were used for measurements.

Code Availability: The custom *EGOTinLiquidSDM* Python package developed for automated data acquisition and subsequent data analysis is available upon reasonable request from the corresponding authors.

Supporting Information

Supporting Information is available from the Wiley Online Library or from the author.

Acknowledgements

This work received funding from the European Union's Horizon 2020 research and innovation program under the Marie Skłodowska-Curie grant agreement No 813863 (BORGES), the EIC Pathfinder PRINGLE project (grant agreement No 101046719), from the Spanish Ministerio de Economıa, Industria y Competitividad, and EU FEDER, through grant no. PID2019-110210GB-I00 (BIGDATASPM), from the Ministerio de Ciencia e Innovacion through grant no. PID2022-142297NB-I00 (BIOMEDSPM40), from the Generalitat de Catalunya through CERCA, and from the ICREA foundation (ICREA Academia award to G.G.). S.T. acknowledges the support from Joerg Barner (JPK) regarding automating the AFM operations. S.R.-M. and M.M.-T. acknowledge MCIN/AEI/10.13039/501100011033/ERDF,UE with project SENSATION PID2022-141393OB-I00, the "Severo Ochoa" Programme for Centers of Excellence in R&D (FUNFUTURECEX2019-000917-S) and Generalitat de Catalunya (2021-SGR-00443).

Conflict of Interest

The authors declare no conflict of interest.

Author Contributions

S.T. led the investigation, designed and developed the automated experimental setup, created the Python data acquisition and data analysis package called *EGOTinLiquidSDM*, proposed high-frequency artifact correction methods, performed all the measurements and data analysis, and drafted the manuscript. R.M.-S. performed the quantitative data analysis based on numerical simulations. S.R.-M. and M.M.-T. designed and fabricated the EGOFET devices. A.K. and G.G. supervised the investigation, managed the project, and edited the manuscript. All authors contributed to the final manuscript.

Data Availability Statement

The data that support the findings of this study are openly available in Zenodo at https://doi.org/10.5281/zenodo.10732680, reference number 10732680.

Keywords

automation, electrolyte-gated organic transistors, nanoscale, operando scanning dielectric microscopy, transistor degradation

Received: March 15, 2024
Revised: June 14, 2024
Published online:

---

[1] E. Macchia, K. Manoli, B. Holzer, C. Di Franco, M. Ghittorelli, F. Torricelli, D. Alberga, G. F. Mangiatordi, G. Palazzo, G. Scamarcio, L. Torsi, *Nat. Commun.* **2018**, *9*, 3223.
[2] B. Burtscher, P. A. Manco Urbina, C. Diacci, S. Borghi, M. Pinti, A. Cossarizza, C. Salvarani, M. Berggren, F. Biscarini, D. T. Simon, C. A. Bortolotti, *Adv. Healthcare Mater.* **2021**, *10*, 2100955.
[3] K. Guo, S. Wustoni, A. Koklu, E. Díaz-Galicia, M. Moser, A. Hama, A. A. Alqahtani, A. N. Ahmad, F. S. Alhamlan, M. Shuaib, A. Pain, I. McCulloch, S. T. Arold, R. Grünberg, S. Inal, *Nat. Biomed. Eng.* **2021**, *5*, 666.
[4] S. Casalini, A. C. Dumitru, F. Leonardi, C. A. Bortolotti, E. T. Herruzo, A. Campana, R. F. de Oliveira, T. Cramer, R. Garcia, F. Biscarini, *ACS Nano* **2015**, *9*, 5051.
[5] A. Spanu, L. Martines, A. Bonfiglio, *Lab Chip* **2021**, *21*, 795.
[6] C. Pitsalidis, A.-M. Pappa, A. J. Boys, Y. Fu, C.-M. Moysidou, D. van Niekerk, J. Saez, A. Savva, D. Iandolo, R. M. Owens, *Chem. Rev.* **2022**, *122*, 4700.
[7] Y. Zhong, A. Saleh, S. Inal, *Macromol. Biosci.* **2021**, *21*, 2100187.
[8] A. Kyndiah, F. Leonardi, C. Tarantino, T. Cramer, R. Millan-Solsona, E. Garreta, N. Montserrat, M. Mas-Torrent, G. Gomila, *Biosens. Bioelectron.* **2020**, *150*, 111844.
[9] A. Kyndiah, M. Dipalo, A. Molazemhosseini, F. A. Viola, F. Modena, G. Iachetta, N. F. Zorn, F. J. Berger, J. Zaumseil, M. Caironi, F. De Angelis, *Sens. Actuators, B* **2023**, *393*, 134227.
[10] S. Löffler, K. Melican, K. P. R. Nilsson, A. Richter-Dahlfors, *J. Intern. Med.* **2017**, *282*, 24.
[11] K. Birmingham, V. Gradinaru, P. Anikeeva, W. M. Grill, V. Pikov, B. McLaughlin, P. Pasricha, D. Weber, K. Ludwig, K. Famm, *Nat. Rev. Drug Discovery* **2014**, *13*, 399.
[12] A. Kyndiah, M. Checa, F. Leonardi, R. Millan-Solsona, M. Di Muzio, S. Tanwar, L. Fumagalli, M. Mas-Torrent, G. Gomila, *Adv. Funct. Mater.* **2021**, *31*, 2008032.
[13] F. Mariani, F. Conzuelo, T. Cramer, I. Gualandi, L. Possanzini, M. Tessarolo, B. Fraboni, W. Schuhmann, E. Scavetta, *Small* **2019**, *15*, 1902534.
[14] R. Giridharagopal, L. Q. Flagg, J. S. Harrison, M. E. Ziffer, J. Onorato, C. K. Luscombe, D. S. Ginger, *Nat. Mater.* **2017**, *16*, 737.
[15] S. Benaglia, S. Drakopoulou, F. Biscarini, R. Garcia, *Nanoscale* **2022**, *14*, 14146.
[16] F. Leonardi, S. Casalini, Q. Zhang, S. Galindo, D. Gutiérrez, M. Mas-Torrent, *Adv. Mater.* **2016**, *28*, 10311.
[17] S. Riera-Galindo, F. Leonardi, R. Pfattner, M. Mas-Torrent, *Adv. Mater. Technol.* **2019**, *4*, 1900104.
[18] A. Pérez-Rodríguez, I. Temiño, C. Ocal, M. Mas-Torrent, E. Barrena, *ACS Appl. Mater. Interfaces* **2018**, *10*, 7296.
[19] J. Smith, W. Zhang, R. Sougrat, K. Zhao, R. Li, D. Cha, A. Amassian, M. Heeney, I. McCulloch, T. D. Anthopoulos, *Adv. Mater.* **2012**, *24*, 2441.
[20] S. Tanwar, R. Millan-Solsona, S. Ruiz-Molina, M. Mas-Torrent, A. Kyndiah, G. Gomila, *Adv. Mater.* **2024**, *36*, 2309767.
[21] J. Guo, L. Q. Flagg, D. K. Tran, S. E. Chen, R. Li, N. B. Kolhe, R. Giridharagopal, S. A. Jenekhe, L. J. Richter, D. S. Ginger, *J. Am. Chem. Soc.* **2023**, *145*, 1866.

[22] L. Q. Flagg, R. Giridharagopal, J. Guo, D. S. Ginger, *Chem. Mater.* **2018**, *30*, 5380.

[23] Z. Ren, Z. Ren, Z. Zhang, T. Buonassisi, J. Li, *Nat. Rev. Mater.* **2023**, *8*, 563.

[24] G. Gramse, M. A. Edwards, L. Fumagalli, G. Gomila, *Appl. Phys. Lett.* **2012**, *101*, 213108.

[25] M. Checa, R. Millan-Solsona, N. Blanco, E. Torrents, R. Fabregas, G. Gomila, *Nanoscale* **2019**, *11*, 20809.

[26] R. Millan-Solsona, M. Checa, L. Fumagalli, G. Gomila, *Nanoscale* **2020**, *12*, 20658.

[27] Q. Zhang, F. Leonardi, S. Casalini, I. Temiño, M. Mas-Torrent, *Sci. Rep.* **2016**, *6*, 39623.